



Numerical Simulation of Horizontal Axis Wind Turbines with Vortex Generators

Hak Min Lee¹ · Oh Joon Kwon¹

Received: 22 June 2018 / Revised: 20 November 2018 / Accepted: 27 November 2018 / Published online: 2 January 2019
© The Korean Society for Aeronautical & Space Sciences 2019

Abstract

In the present study, a simulation about the effects of vortex generators on horizontal axis wind turbine rotor blade was numerically conducted using a static coupled CFD–CSD method. A Navier–Stokes CFD flow solver based on unstructured meshes was used to obtain the blade aerodynamic loads. A FEM-based CSD solver employing a nonlinear coupled flap-lag-torsion beam theory was utilized to calculate the blade elastic deformation. The coupling of the CFD and CSD solvers was accomplished in a loosely coupled manner by exchanging the information between the two solvers at infrequent intervals. The static coupled CFD–CSD method was applied to the NREL 5 MW reference wind turbine rotor under steady axial flow conditions. Triangular counter-rotating vortex generators were adopted to control flow separation and radial flow in the inboard section of the NREL 5 MW reference rotor blades. They were installed on the inboard part of the blade from 0.2 to 0.4 R. As a result of the flow analysis considering the counter-rotating vortex generators, strong vortices were generated by counter-rotating vortex generators. It can be seen that the regions where flow separation and radial flow occur in the inboard sections were reduced compared to the baseline wind turbine. For this reason, the maximum power improvement due to counter-rotating vortex generators was 1.04% at the rated wind speed.

Keywords Computational fluid dynamics · Computational structural dynamics · Horizontal axis wind turbine · Vortex generators

List of Symbols

C_p	Surface pressure coefficient
c	Blade chord length
F_n	Sectional normal forces, N/m
F_t	Sectional tangential forces, N/m
R	Rotor radius of blade
u	Spanwise deflection
v	Lead-lag deflection
w	Flap bending deflection
θ	Rigid pitch angle, degree
ϕ	Torsional deformation at elastic axis, degree
Ω	Rotor rotational speed
β_p	Precone angle, degree
\vec{Q}	Vector of conservative variables

\vec{F}, \vec{G}	Flux vectors
\vec{n}	Normal vector
\tilde{K}	Preconditioning matrix
U	Strain energy
T	Kinetic energy
W	Virtual energy
M	Mass matrix
G	Gyroscopic matrix
K	Stiffness matrix

1 Introduction

Over the past decades, wind turbine rotor blades have been becoming more and more larger to produce more power and reduce facility construction cost. For large-scale wind turbine rotor blades, the thickness ratio of inboard airfoils corresponds to 30–40% of the chord length to withstand blade loading. With the high aerodynamic efficiencies of modern wind turbine rotor blades, the power loss of wind turbine

✉ Oh Joon Kwon
ojkwon@kaist.ac.kr

¹ Department of Aerospace Engineering, Korea Advanced Institute of Science and Technology, Daejeon 34141, Republic of Korea

rotor blades occurs due to the flow separation and radial flow generated in the inboard sections [1].

Recently, researchers have shown interest in reducing the power loss of wind turbine rotor blades. Chow et al. [1] installed various fence configurations on the inboard section of the NREL 5 MW rotor to limit the radial flow component and minimize flow separation to increase rotor power. They investigated the aerodynamic characteristics of the NREL 5 MW rotor according to fence height and position change.

Among flow control techniques, vortex generators are popularly employed because it is easy to install and effective to delay flow separation. Vortex generators are aerodynamic devices that vary in shape and arrangement. They create streamwise vortices that mix the high momentum of the outer region into the low momentum region near the surface, making the flow more resistant to separation in an adverse pressure gradient. For DU 30 airfoil used on the inboard section of the NREL 5 MW rotor, Timmer and van Rooij [2] performed the wind tunnel test to investigate the vortex generator effect. As a result, trailing edge separation is suppressed and the stalling process of the DU 30 airfoil is delayed. Also, the effects of vortex generators on newly designed in-house thick wind turbine CAS airfoil series were investigated by Zhang et al. [3].

Through numerical simulations as well as experiments, studies on the vortex generator were performed. Sorensen et al. [4] carried out numerical simulations of FFA-W3-301 and FFA-W3-360 with varying vortex generator positions. Troldborg et al. [5] compared the results of numerical simulations of DTU 10 MW wind turbines with and without vortex generators installed on the inboard part of the blade. Vortex generators were modeled using the BAY model instead of fully gridded CFD. The simulations on the DTU 10 MW turbine showed that vortex generators may effectively delay flow separation and therefore can improve the aerodynamic characteristics of the inner part of the blade. Additionally, the influence of different vortex generator configurations on the DTU 10 MW rotor performance was investigated [6].

Florentie et al. [7] conducted numerical studies on vortex generators using body fitted mesh method and source term models. Flow analysis was performed on the flat plate and airfoil, and the results were compared according to each method. Although the direction and magnitude of the force are slightly different from the body-fitted mesh method, the source term models represent the vortex generator characteristics well.

Tian et al. [8] studied the application of an array of vortex generators to control flow separation and alleviate blade contamination problems of wind turbines. Blade element method (BEM) computations were carried out to determine the aerodynamic rotor performance. The case study of an NREL 5 MW wind turbine demonstrated that total power loss per year due to the leading edge contamination could go

up to 6.6%. It suggested that vortex generators could be used to improve wind turbine performance and increase annual energy production (AEP) by 1% by delaying the flow separation and mitigating the soiling effect.

Numerical studies with vortex generators are mostly limited to two-dimensional airfoils. In addition, BEM computations were performed to predict the aerodynamic performance of wind turbine blades considering vortex generators. Since this method is a two-dimensional analysis, it is difficult to accurately predict the three-dimensional flow separation near the root of the wind turbine. Prediction of the accurate flow separation area is necessary to understand the effect of vortex generators on wind turbine performance. To predict the accurate flow separation, the three-dimensional CFD method is essential. For large wind turbines, the structural deformation is significant, thus affecting the flow separation region. Therefore, it should be accompanied by the CSD analysis.

In the present study, the flow analysis was performed to investigate the change of flow characteristics according to vortex generators on the wind turbine rotor blade using a coupled CFD–CSD method. A Navier–Stokes CFD flow solver based on unstructured meshes was used to obtain the blade aerodynamic loads. The blade elastic deformation was calculated using a FEM-based CSD solver which employs a nonlinear coupled flap-lag-torsion beam theory. Validation of the CFD–CSD coupled method was made for the NREL 5 MW reference rotor blade under steady axial flow conditions. Vortex generators were used to improve the performance of the NREL 5 MW reference rotor blade, and counter-rotating vortex generators, which are known to be effective among various vortex generators, were applied [9, 10]. Counter-rotating vortex generators were installed in the region where flow separation and radial flow occurred. The flow characteristics of the NREL 5 MW reference rotor blade with and without vortex generators were compared.

2 Numerical Method

2.1 CFD Solver

An incompressible Navier–Stokes CFD solver based on unstructured meshes was utilized to analyze the flow around NREL 5 MW reference wind turbine rotor [11]. The equations for wind turbine applications are the corresponding incompressible equations with an artificial compressibility method [12] as:

$$\begin{aligned} \frac{\partial}{\partial t^*} \int_V \vec{Q} dV + \tilde{K} \frac{\partial}{\partial t} \int_V \vec{Q} dV + \oint_{\partial V} \vec{F}(\vec{Q}) \cdot \vec{n} dS \\ = \oint_{\partial V} \vec{G}(\vec{Q}) \cdot \vec{n} dS, \end{aligned} \quad (1)$$

where \vec{Q} is the solution vector of primitive variables. $\vec{F}(\vec{Q})$ and $\vec{G}(\vec{Q})$ represent the inviscid and viscous fluxes of these variables, respectively. \tilde{K} is the preconditioning matrix introduced to accommodate the artificial compressibility into the governing equations. A node-based unstructured finite-volume method (FVM) was used for the discretization of the governing equations. The computational domain consists of a finite number of median-dual control volumes formed by connecting the cell centroid, face and edge midpoints of all cells sharing the particular node. The convective flux terms were computed by Roe’s flux difference splitting method [13], while the diffusive ones were calculated based on a modified central differencing [14]. The time integration was made implicitly using the linearized Euler backward differencing. The point Gauss–Seidel method was used to solve the linear system of equations at each time step. The correlation-based transition $k - \omega$ SST model [15] was used to estimate the turbulent eddy viscosity considering the laminar–turbulent transition effect. To consider mesh movement by blade deformation, mesh deformation techniques were used [16, 17].

For boundary conditions, the no-slip boundary condition was applied on the rotor blade surface. At the inflow boundary, the flow variables were set to the freestream values, and at the far-field boundary, the characteristic boundary condition with the Riemann invariants was applied. Since the rotor has periodicity between the blades under axial flow conditions, calculations were made for a single rotor, and the periodic boundary condition was imposed between the other blades. The flow solver was parallelized using MeTiS and MPI libraries to reduce the flow analysis time.

2.2 CSD Solver

The blade structure was modeled as a nonlinear Euler–Bernoulli cantilever beam subjected to spanwise deflection, lead-lag bending, flap bending, and torsional deformation [11]. The blade deformation was assumed to be moderate, retaining the geometric nonlinearities up to second order [18]. The equations of motion were derived based on Hamilton’s principle. Figure 1 shows the blade coordinate frame and the blade deformation kinematics. The rectangular coordinate system x, y, z is attached to the undeformed blade. The x axis is the same as the elastic axis, and the y axis indicated the leading edge. When the blade deforms, the point P on the undeformed elastic axis is shifted to the point P' by axial deflection, lead-lag bending, flap bending, in the x, y, z directions, respectively. Then, the blade cross-section containing P' experiences rotations of rigid pitch and elastic torsion regarding the deformed elastic axis.

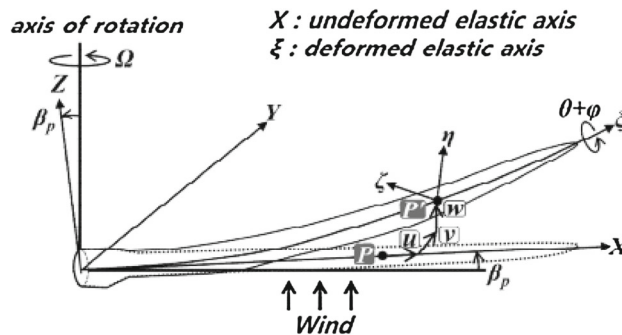


Fig. 1 Coordinate system and deformation kinematics

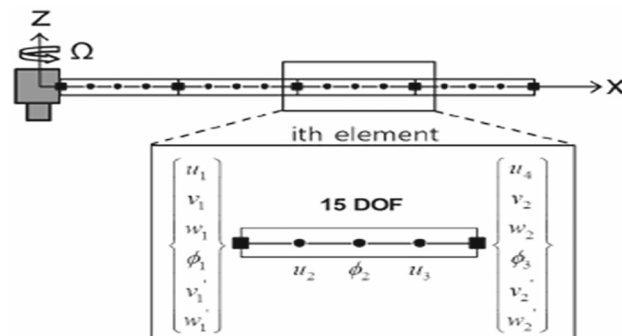


Fig. 2 Finite element showing nodal degrees of freedom

The discretized governing equations of the blade elastic motion were obtained using a finite-element method. The blade is divided into a number of finite elements, and each element involves 15 nodal degrees of freedom as shown in Fig. 2. The distribution of deformation over each element can be represented by appropriate interpolating polynomials. In the present study, the Hermite polynomial was used for the lead-lag and flap bending deflections to secure the continuity of both displacement and slope between the elements. For the axial and elastic torsion deformations, the Lagrangian polynomial was used to guarantee the displacement continuity. The discretized form of the model can be written as:

$$\int_{t_2}^{t_1} \left[\sum_{i=1}^N \delta U_i - \delta T_i - \delta W_i \right] dt = 0. \tag{2}$$

Here, the subscript i denotes the i th beam element, and N is the total number of finite elements on the blade. δU_i , δT_i and δW_i are the variation of strain energy, the variation of kinetic energy, and the virtual work done by the external aerodynamic loads, respectively. After applying the interpolating polynomials, these elemental energy variations can be expressed in the following matrix form in terms of the nodal displacement, q_i , as:

$$M_i \ddot{q}_i + G_i \dot{q}_i + K_i q_i = F_{0,i} + F_{NL,i} + F_{aero,i} \\ q_i^T = \{u_1, v_1, w_1, \phi_1, v_1', w_1', u_2, \phi_2, u_3, u_4, v_2, w_2, \phi_3, v_2', w_2'\}_i, \tag{3}$$

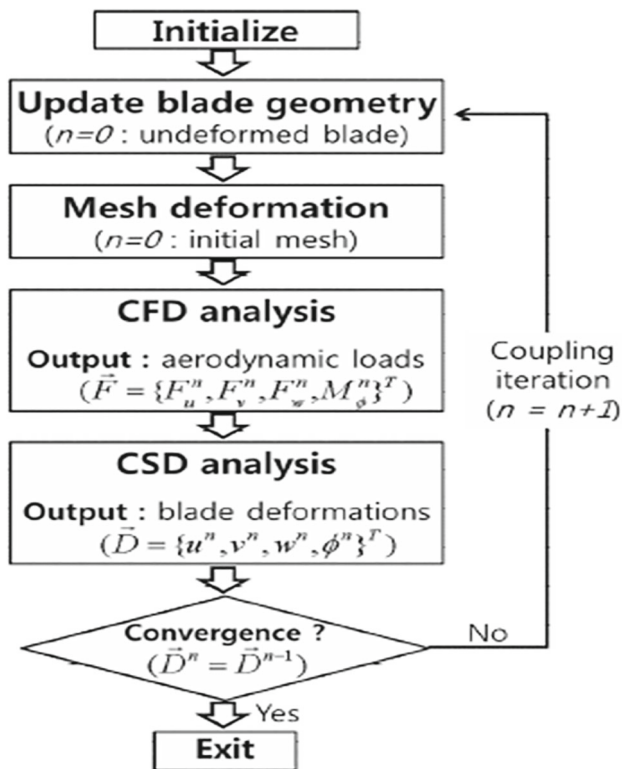


Fig. 3 Static coupled CFD–CSD analysis

where M_i , G_i and K_i are the elemental mass, gyroscopic, and stiffness matrices, respectively, and $F_{0,i}$ and $F_{NL,i}$ are the elemental constant and nonlinear vectors. $F_{aero,i}$ indicates the applied aerodynamic loads acting on the i th element of the blade, which is to be provided from the CFD calculation. The finite element assembly process for the elemental matrices and vectors was utilized to obtain the global nonlinear equations of motion of the blade. The equation is as follows:

$$M\ddot{q} + G\dot{q} + Kq = F_0 + F_{NL} + F_{aero}. \quad (4)$$

When the turbine rotor operates at axial flow conditions, the blade airload remains unchanged, so Eq. (4) can be reduced to static equilibrium equations by ignoring the time derivative terms as:

$$Kq = F_0 + F_{NL} + F_{aero}. \quad (5)$$

2.3 CFD–CSD Coupling Method

Figure 3 shows the entire procedure for the static CFD–CSD coupling. Initially, the CFD simulation is performed on the initial mesh for the undeformed blade. Once the flow solution converges to a steady state, the cross-sectional airload at each spanwise position is calculated as the pressure and skin friction on the surface, which is provided to the CSD solver. The

blade elastic deformation is calculated using Eq. (5). In consideration of the blade elastic deformation, the CFD mesh points are newly constructed using the mesh deformation techniques. Using such a newly constructed computational mesh, flow simulation is performed again to calculate the sectional aerodynamic loading on the deformed blade. This iteration is conducted until a converged static equilibrium blade deformation is obtained.

3 Results and Discussion

3.1 NREL 5 MW Reference Wind Turbine

To capture the flow separation occurring at the NREL 5 MW reference rotor blade, the flow analysis was performed and the results were compared with those of other researchers. This wind turbine configuration consists of three blades, which control the power through various speeds and pitch angles. It has a power rating of 5 MW at the rated wind speed of 11.5 m/s. The rotor has a radius of 63 m and uses a series of DU airfoils except the NACA 64–618 airfoil section at the outboard region. The blade is set at a precone angle of 2.5°.

In Fig. 4, the computational mesh was generated to perform the flow analysis for the NREL 5 MW reference wind turbine. A single blade grid was constructed by applying the periodic boundary condition. To capture the boundary layer on the blade surface more accurately, a hybrid mesh topology was used as shown in Fig. 4b. A total of 32 layers of prismatic cells were packed on the blade surface with a stretching ratio of 1.28, and the remaining flow domain was filled with tetrahedral cells. The computational mesh contains approximately 5.4 M prismatic cells and 2.9 M tetrahedral cells, and the number of nodes is about 3.2 M. For the CSD calculations, 49 finite elements were used along the span to model the structure of the blade. The elastic axis was assumed to be located at 1/4-chord as reported by NREL [19].

Initially, the CFD calculation for the NREL 5 MW reference wind turbine was performed at the rated wind speed of 11.5 m/s. The CFD–CSD calculation was performed until the difference in the blade deformations was less than 0.2%. In Fig. 5, the history of blade tip deformations during the CFD–CSD coupled iteration is presented. It can be seen that the calculation converges in the fourth iteration. To investigate the performance of the rotor blade aerodynamic loads, additional CFD–CSD coupled calculations were made at the wind speeds of 4, 6, 8, 10, 15 and 20 m/s. The rotor speed controls are based on the data reported by NREL [19], whereas the pitch control angles at the wind speeds above the rated were predicted based on the results of the present CFD–CSD coupled calculations. Table 1 shows the rotational speed of

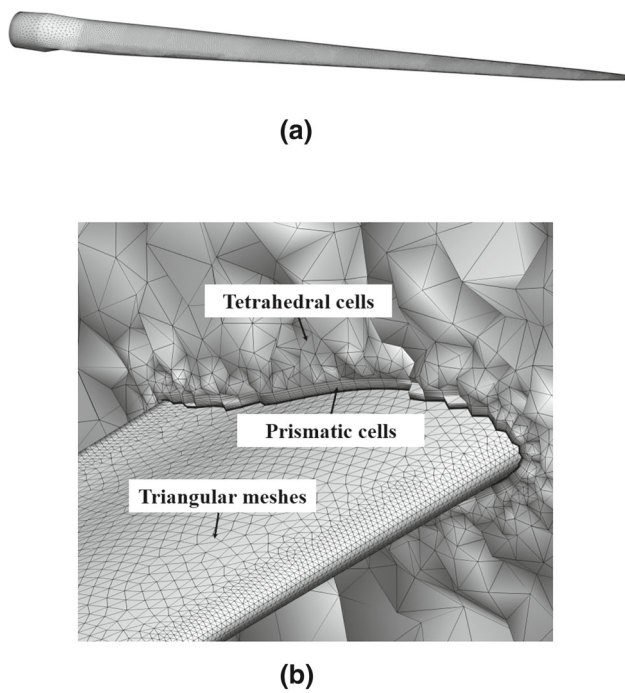


Fig. 4 Computational mesh for the CFD calculation. a Surface mesh. b Hybrid mesh topology. c Boundary conditions

the NREL 5 MW reference wind turbine according to wind speed.

In Fig. 6, the predicted flapping deflection and rotor torque are presented for the various wind speeds. In the region controlled by the rotational speed, the torque increases as the wind speed increases, and the torque is maintained constant in the region controlled by the pitch control. The present CFD–CSD coupled results compare very well with the FAST-Aerodyn results [19].

The streamlines on the blade surface are presented as shown in Fig. 7. The flow separation and radial flow occur in the inboard part of the NREL 5 MW reference rotor. As

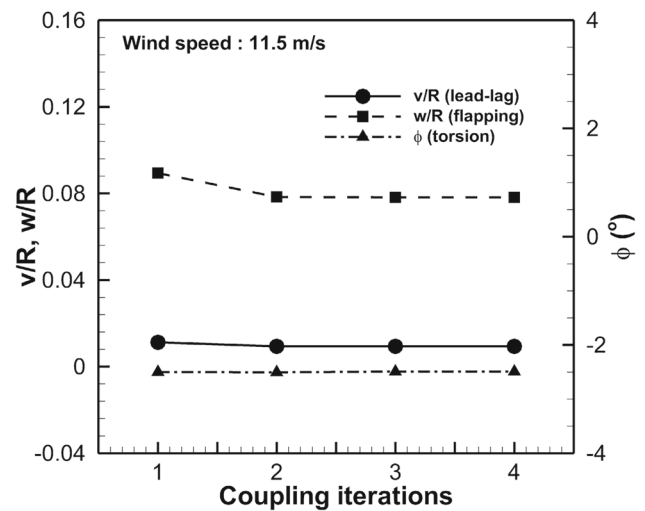


Fig. 5 History of blade tip deformation

Table 1 Rotational speed for steady axial flow conditions

Wind speed (m/s)	RPM
4	7.2
6	7.9
8	9.2
10	11.4
11.5	12.1
15	12.1
20	12.1

rotational speed of the wind turbine increases, the area of the flow separation and radial flow becomes larger. In case of the rated wind speed of 11.5 m/s, the flow separation and radial flow occur approximately up to 0.4 R of the blade. As the pitch control is applied, it can be seen that the area of the flow separation and radial flow are reduced compared to that of the rated wind speed of 11.5 m/s.

3.2 Vortex Generator

As can be seen in Fig. 8, the counter-rotating vortex generators were adopted to improve the wind turbine performance. They are more effective in controlling the flow separation than co-rotating vortex generators [9, 10]. Counter-rotating vortex generators used in the DTU 10 MW reference wind turbine were applied [5] as shown in Fig. 8. The parameters of them are presented in Table 2, and the maximum chord length (c_{max}) of the NREL 5 MW reference wind turbine rotor blade is about 4.64 m. Based on the flow analysis results at the rated wind speed of 11.5 m/s where the region of flow separation and radial flow is the widest, counter-rotating vortex generators were installed. The counter-rotating vortex generators were located linearly between the chordwise position of 0.5 c

Fig. 6 Flapping deflection and torque for various wind speeds. **a** Flapping deflection. **b** Torque

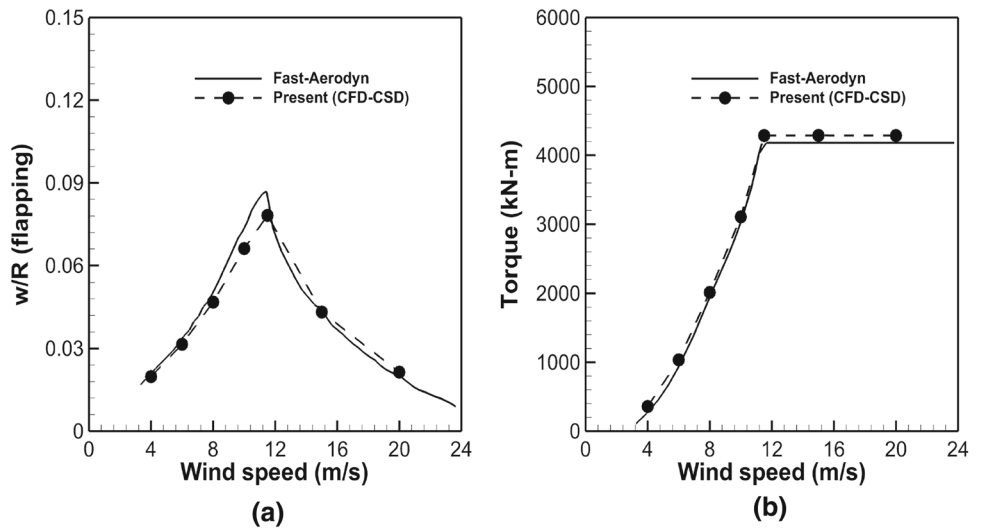


Fig. 7 Streamlines on the surface for various wind speeds

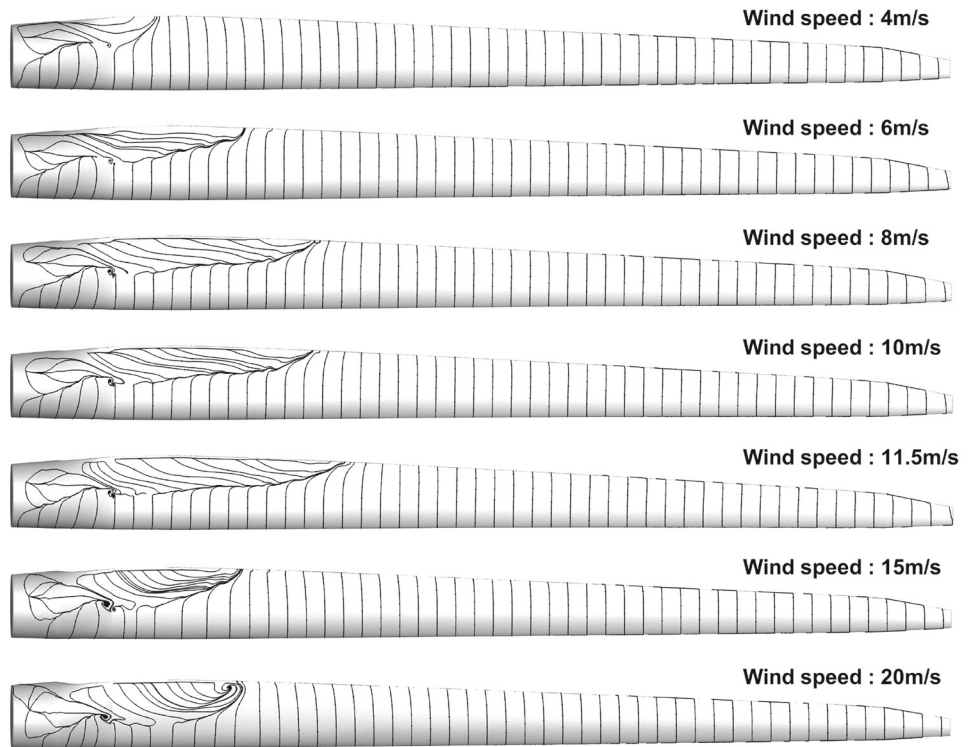


Fig. 8 Configuration of counter-rotating vortex generator. **a** Side view. **b** Top view

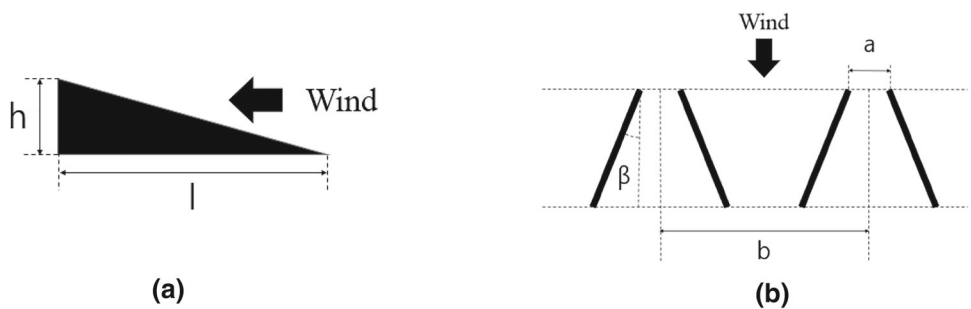
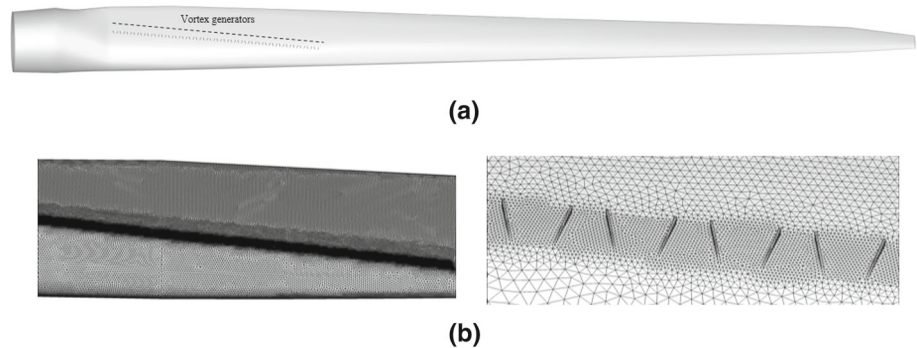


Table 2 Parameters of counter-rotating vortex generators

h	l	a	b	β
0.01 c_{\max}	0.04 c_{\max}	0.045 c_{\max}	0.055 c_{\max}	16°

Fig. 9 Blade surface with counter-rotating vortex generators. **a** Solid modeling with counter-rotating vortex generators. **b** Surface mesh near counter-rotating vortex generators

at the spanwise position of 0.2 R and the chordwise position of 0.2 c at the spanwise position of 0.4 R. A total of 30 pairs of counter-rotating vortex generators were installed in the inboard section of the NREL 5 MW wind turbine blade.

3.3 Flow Analysis with Counter-Rotating Vortex Generators

The surface modeling was performed to conduct the flow analysis of the NREL 5 MW reference rotor blade considering counter-rotating vortex generators as shown in Fig. 9a. To capture the vortices generated by counter-rotating vortex generators, the grid was densely constructed in the place where they were installed. The computational mesh for the flow analysis contains approximately 6.7 M prismatic cells and 4.9 M tetrahedral cells, and the number of nodes is about 4.3 M. The surface mesh near counter-rotating vortex generators is presented in Fig. 9b. The boundary conditions are given same as shown in Fig. 4c.

In Fig. 10, the streamlines on the blade surface with counter-rotating vortex generators are presented. It is shown that due to counter-rotating vortex generators, the areas where flow separation and radial flow occur are reduced. In particular, the effect of counter-rotating vortex generators is largest at the wind speed of 11.5 m/s, and the area of flow separation and radial flow decreases from 0.4 to 0.3 R position of the blade. As shown in Fig. 11, the strong vortices were created by counter-rotating vortex generators. The high momentum of the outer region is mixed with the low momentum region near the surface, making the flow more resistant to separation at the adverse pressure gradient.

In Fig. 12, the chordwise surface pressure contours with and without counter-rotating vortex generators are extracted at 0.35 R, 0.60 R and 0.9 R point of the blade at the rated wind speed of 11.5 m/s. At the 0.35 R where counter-rotating vortex generators are installed, the suction peak is increased,

and the strong vortices generated by counter-rotating vortex generators cause the flow to attach to the surface. For this reason, the force generated by the pressure difference between the upper surface and the lower surface of the airfoil increases. In addition, vortex generators affect not only the inboard region, but also the outer region. At 0.9 R position of the blade, the suction peak is slightly decreased compared to the case without vortex generators.

Since the flow characteristics are changed in the inboard region by the effect of counter-rotating vortex generators, it affects the blade deformations. Figure 13 shows the blade deformations in the spanwise direction with and without vortex generators at the rated wind speed of 11.5 m/s. As the force acting on the inboard section is increased by counter-rotating vortex generators, the lead-lag, flapping and torsion deformation are slightly larger compared to the results without counter-rotating vortex generators. Especially, it is shown that at 0.9 R location of the blade, due to the slight increase of the nose down torsional deformation compared to the case without vortex generators, the suction peak decreases as above mentioned.

Figure 14 compares the normal and tangential forces along the span of the blade from 0.2 to 1.0 R with and without vortex generators. The tangential and the normal forces are increased in the inboard section by counter vortex generators at the wind speeds of 4, 6, 8, 10, 11.5, 15 and 20 m/s. The tangential and normal forces are increased the most at the rated wind speed of 11.5 m/s.

In Fig. 15, the flap bending moment and power are compared with and without vortex generators. Due to the increase of normal force and tangential force by vortex generators, the flap bending moment and power increase. For a flap bending moment, it increases approximately 0.06, 0.24, 0.30, 0.37, 0.45, 0.17 and 0.31% at wind speeds of 4, 6, 8, 10, 11.6, 15, and 20 m/s. The power due to vortex generators increases

Fig. 10 Streamlines on the surface with counter-rotating vortex generators for various wind speeds

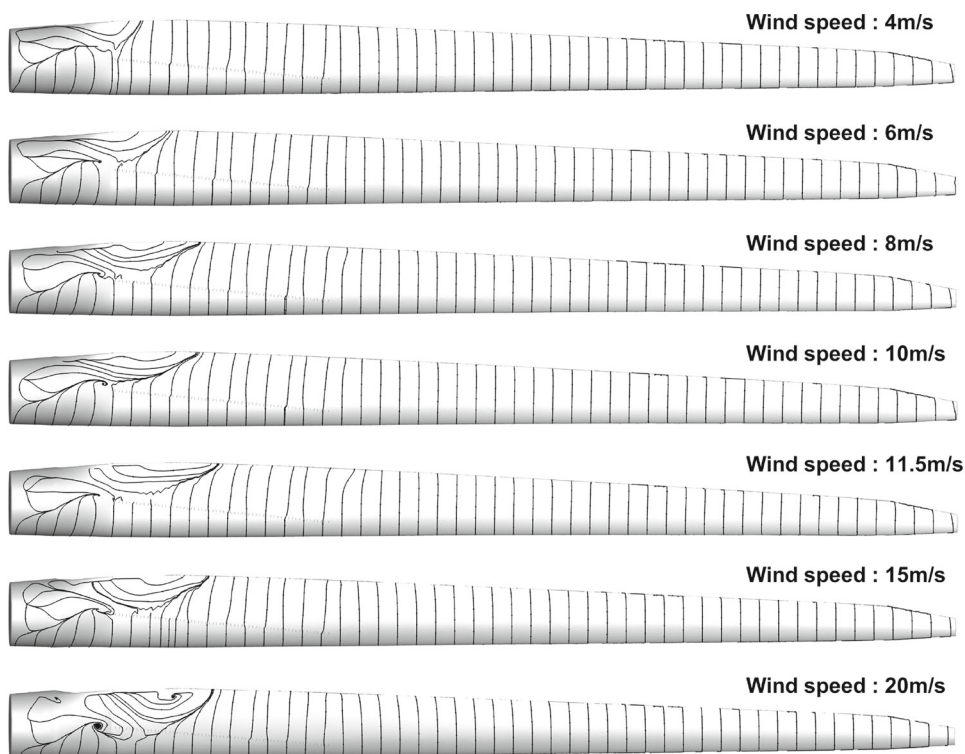


Fig. 11 Vorticity contours in the inboard section at the rated wind speed of 11.5 m/s. **a** Without vortex generators. **b** With vortex generators

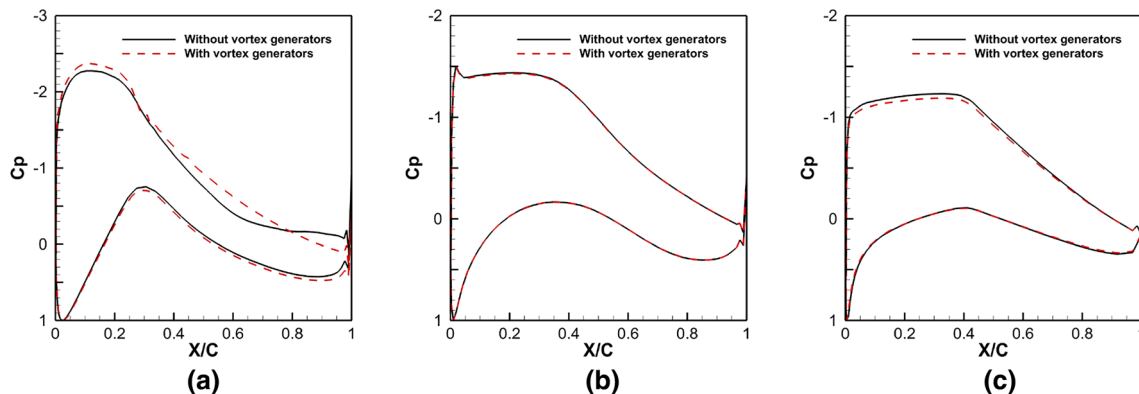
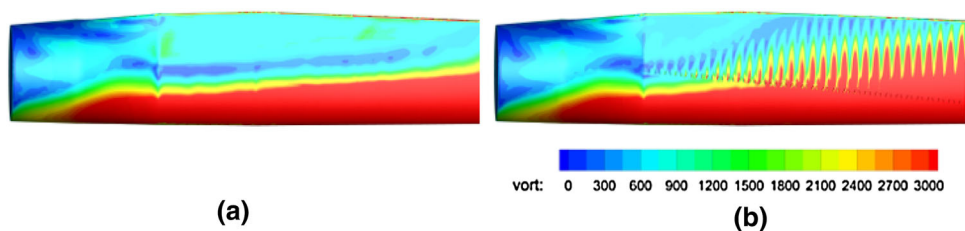


Fig. 12 Chordwise surface pressure distribution with and without counter-rotating vortex generators at the rated wind speed of 11.5 m/s. **a** 0.35R. **b** 0.60R. **c** 0.90R

about 0.02, 0.50, 0.89, 0.86, 1.04, 0.51 and 0.80% at wind speeds of 4, 6, 8, 10, 11.6, 15, and 20 m/s.

4 Conclusion

In the present study, a simulation about the effects of vortex generators on horizontal axis wind turbine rotor blades was numerically conducted using a coupled CFD–CSD method. The blade load was calculated using CFD solver based on

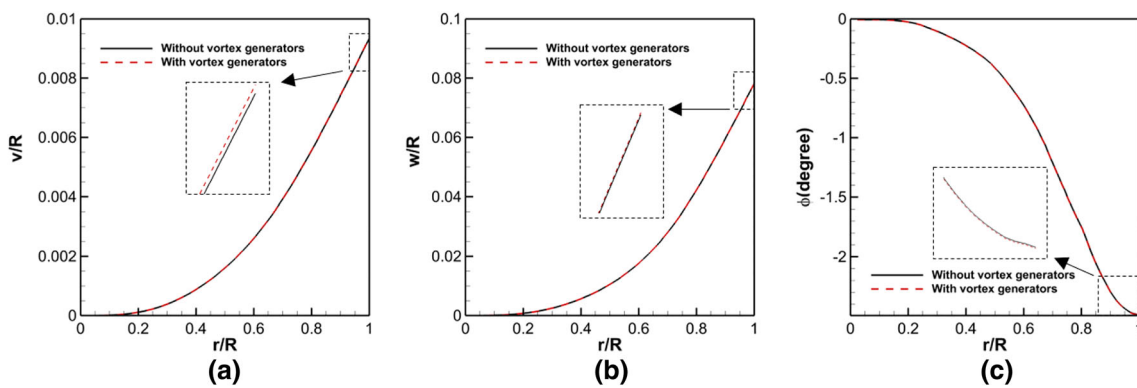
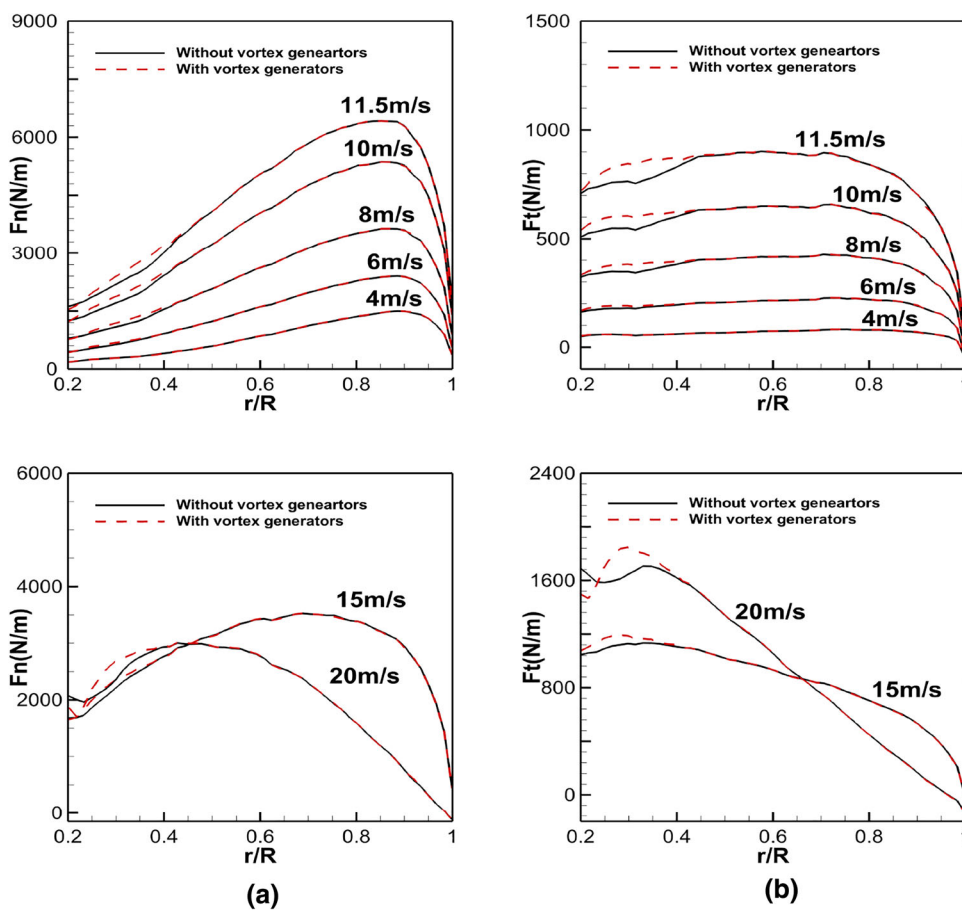


Fig. 13 Spanwise distribution of blade deformations with and without counter-rotating vortex generators at the rated wind speed of 11.5 m/s. **a** Lead-lag deflection. **b** Flapping deflection. **c** Torsional deflection

Fig. 14 Spanwise distribution of normal and tangential force with and without counter-rotating vortex generators at various wind speeds. **a** Normal force. **b** Tangential force



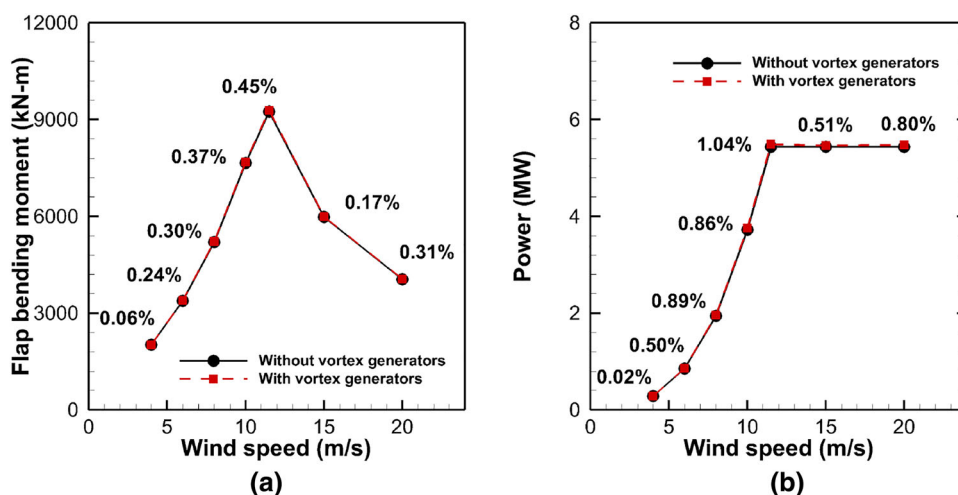
unstructured meshes. A FEM-based CSD solver based on a nonlinear coupled flap-lag-torsion beam theory was used to obtain the blade elastic deformation. The coupling of the CFD and CSD solvers was accomplished in a loosely coupled manner.

Validation of the CFD–CSD coupled method was made for the NREL 5 MW reference rotor blade under steady axial flow conditions. It was found that the results are in good agreement with those of other researchers. Through

the flow analysis, it is shown that the flow separation and radial flow occur in the inboard region. Based on this, counter-rotating vortex generators, which are known to have a good flow control effect, were installed in the inboard area.

As a result of flow analysis of the NREL 5 MW reference wind turbine rotor blade considering counter-rotating vortex generators, flow separation is delayed due to strong vortices generated by counter-rotating vortex generators, and

Fig. 15 Flap bending moment and power for various wind speeds. **a** Flap bending moment. **b** Power



the areas where flow separation and radial flow occur are reduced. The lead-lag, flapping and torsional deformations are slightly increased by counter-rotating vortex generators. It is confirmed that the normal and tangential force acting on the blade in the inboard region where counter-rotating vortex generators are applied are increased by the effect of counter-rotating vortex generators. For this reason, the power and flap bending moment due to the vortex generators increases at wind speeds of 4, 6, 8, 10, 11.5, 15 and 20 m/s.

Acknowledgements This work was supported by the New and Renewable Energy Core Technology Program of the Korea Institute of Energy Technology Evaluation and Planning (KETEP), and financial resource was granted by the Ministry of Trade, Industry and Energy, Republic of Korea (no. 20153030023880). This research was also supported by the Climate Change Research hub of KAIST (Grant no. N11180110).

References

- Chow R, van Dam CP (2011) Inboard stall and separation mitigation techniques on wind turbine rotors. In: 49th AIAA aerospace science meeting including the new horizons forum and aerospace exposition, Orlando, Florida, 2011. <https://doi.org/10.2514/6.2011-152>
- Timmer WA, van Rooij RPJOM (2003) Summary of the Delft University wind turbine dedicated airfoils. *J Sol Energy Eng* 125(4):488–496. <https://doi.org/10.1115/1.1626129>
- Zhang L, Li X, Yang K, Xue D (2016) Effects of vortex generators on aerodynamic performance of thick wind turbine airfoils. *J Wind Eng Ind Aerodyn* 156:84–92. <https://doi.org/10.1016/j.jweia.2016.07.013>
- Sorensen NN, Zahle F, Bak C, Vronsky T (2014) Prediction of the effect of vortex generators on airfoil performance. *J Phys Conf Ser* 524. <https://doi.org/10.1088/1742-6596/524/012019>
- Troldborg N, Zahle F, Sorensen NN (2015) Simulations of a MW rotor equipped with vortex generators using CFD and an actuator shape model. In: 53rd AIAA aerospace sciences meeting, Florida, 2015. <https://doi.org/10.2514/6.2015-1035>
- Troldborg N, Zahle F, Sorensen NN (2016) Simulations of wind turbine rotor with vortex generators. *J Phys Conf Ser* 753. <https://doi.org/10.1088/1742-6596/753/022057>
- Florentie L, van Zuijlen AH, Hulshoff SJ, Bijl H (2017) Effectiveness of side force models for flow simulations downstream of vortex generators. *AIAA J*. <https://doi.org/10.2514/1.j055268>
- Tian QQ, Corson D, Baker JP (2016) Application of vortex generators to wind turbine blades. In: 34th wind energy symposium AIAA SciTech Forum, 2016. <https://doi.org/10.2514/6.2016-0518>
- Wendt BJ, Hingst WR (1994) Flow structure in the wake of a wish-bone vortex generator. *AIAA J* 32(11):2234–2240. <https://doi.org/10.2514/3.12282>
- Dai L, Zhang H, Jiao J, Li X, Kang S (2013) Characterization of vortex generators induced flow around wind turbine airfoil. *Appl Mech Mater* 447–453:1779–1784. <https://doi.org/10.4028/www.scientific.net/AMM.448-453.1779>
- Yu DO, Lee HM, Kwon OJ (2016) Aerodynamic shape optimization of wind turbine rotor blades considering aeroelastic deformation effect. *J Mech Sci Technol* 30(2):705–718. <https://doi.org/10.1007/s12206-016-1026-5>
- Chorin AJ (1997) A numerical method for solving incompressible viscous flow problems. *J Comput Phys* 135(135):118–125. <https://doi.org/10.1006/jcph.1997.5716>
- Roe PL (1981) Approximate Riemann solver, parameter vectors and difference. *J Comput Phys* 43(2):357–372. [https://doi.org/10.1016/0021-9991\(81\)90128-5](https://doi.org/10.1016/0021-9991(81)90128-5)
- Mathur SR, Murthy JY (1997) A pressure-based method for unstructured meshes. *Numer Heat Transf Part B* 31(2):195–215. <https://doi.org/10.1080/10407799708915105>
- Langry RB, Menter FR (2009) Correlation-based transition modeling for unstructured parallelized computational fluid dynamics codes. *AIAA J* 47(12):2894–2906. <https://doi.org/10.2514/1.42362>
- Bottasso CL, Dentomi D, Serra R (2005) The ball-vertex method: a new simple spring analogy method for unstructured dynamic meshes. *Comput Methods Appl Mech* 194(39):4244–4264. <https://doi.org/10.1016/j.cma.2004.08.014>
- Kholodar DB, Morton SA, Cummings RM (2005) Deformation of unstructured viscous grids. In: 43rd AIAA aerospace sciences meeting and exhibit, Reno, Nevada, 2005. <https://doi.org/10.2514/6.2005-926>
- Hodges DH, Dowell EH (1974) Nonlinear equations of motion for the elastic bending and torsion of twisted nonuniform rotor blades. *NASA TN D-7818*
- Jonkman JM, Butterfield S, Musial W, Scott G (2009) Definition of a 5-MW reference wind turbine for offshore system development. *NREL/TP-500-38060*